Micromagnetic studies of three-dimensional pyramidal shell structures

A Knittel[1], M Franchin[1], T Fischbacher[1], F Nasirpouri[3], S J Bending[2] and H Fangohr[1]

[1] School of Engineering Sciences, University of Southampton, Southampton SO17 1BJ, UK

[2] Department of Physics and Astronomy, University of Bath, BA2 7AY, UK

[3] Department of Materials Engineering, Sahand University of Technology, Tabriz 51335-1996, Iran

E-mail: `fangohr@soton.ac.uk`

Abstract. We present a systematic numerical analysis of the magnetic properties of pyramidal-shaped core-shell structures in a size range below 400 nm. These are three-dimensional structures consisting of a ferromagnetic shell which is grown on top of a non-magnetic core. The standard micromagnetic model without the magnetocrystalline anisotropy term is used to describe the properties of the shell. We vary the thickness of the shell between the limiting cases of an ultra-thin shell and a conventional pyramid and delineate different stable magnetic configurations. We find different kinds of single-domain states, which predominantly occur at smaller system sizes. In analogy to equivalent states in thin square films we term these onion, flower, C and S states. At larger system sizes, we also observe two types of vortex states, which we refer to as symmetric and asymmetric vortex states. For a classification of the observed states, we derive a phase diagram that specifies the magnetic ground state as a function of structure size and shell thickness. The transitions between different ground states can be understood qualitatively. We address the issue of metastability by investigating the stability of all occurring configurations for different shell thicknesses. For selected geometries and directions hysteresis measurements are analysed and discussed. We observe that the magnetic behaviour changes distinctively in the limit of ultra-thin shells. The study has been motivated by the recent progress made in the growth of faceted core-shell structures.

PACS numbers: 75.75.Fk, 75.60.Jk, 75.78.Cd

This article has been published in A Knittel *et al* 2010 *New J. Phys* **12** *113048*

.

1. Introduction

The magnetocrystalline anisotropy of a bulk magnetic material governs its magnetic behaviour and is therefore key to its technological applicability. However, it is an intrinsic property of the material and cannot readily be tailored [1]. In contrast, the magnetic behaviour of a nanomagnet is also largely influenced by the interaction of the magnetization with its shape. This dependency provides the possibility of fine-tuning magnetic properties through shape-manipulation, which in turn requires very precise growth techniques.

Lithographic methods have been widely used to produce ordered arrays of nanoelements [2]. The basic idea is to deposit a thin resist layer onto a substrate, parts of which are then chemically altered by exposing them to radiation. Finally, different techniques are used in order to transfer the generated pattern into an array of nanoelements. However, these nanoelements are not very well defined along the direction perpendicular to the original resist layer. In contrast, chemical methods are based on what is often referred to as the 'bottom up' approach, i.e. the nanoparticles develop from smaller units. The challenge of fabricating nanoparticles of non-spherical geometry is, therefore, to obtain a suitably anisotropic growth. Corresponding research on magnetic nanoparticles has led to the growth of a wide variety of shapes for hard magnetic iron compounds [3, 4].

In this paper, we use the micromagnetic model in the limit of soft magnetic materials (thus neglecting the magnetocrystalline anisotropy of nickel), which allows us to accurately analyse the competition between the exchange and the magnetostatic contributions of the model. Due to their nonlinearity, analytical approaches to solving the micromagnetic equations are feasible only for highly symmetric geometries and, even in these cases, cannot address certain phenomena such as metastability. Therefore, one usually employs numerical methods such as the finite difference (FD) method or the finite element (FE) method. The disadvantage of numerical results is that they generally give less physical insight than a corresponding analytical solution. However, micromagnetic simulations do not only yield the magnetization but also other important scalar and vector fields such as energy densities and effective magnetic fields corresponding to the different energetic contributions. A careful examination of these fields can reveal much about the underlying physical mechanisms.

Micromagnetic studies of fundamental geometries have been mostly carried out for platelets, either of square [5, 6, 7, 8] or circular [9, 10, 8] shape, and ferromagnetic cubes [11, 12]. Due to the above-mentioned limitations of standard growth techniques, more complex, three-dimensional (3D) nanoelements have been subject to far less research. Corresponding micromagnetic studies are also more involved as a standard FD discretization is only accurate for structures of rectangular symmetry [13]. In the literature, one can find micromagnetic investigations of cones [14, 15], pyramids [14], partially spherical structures [16, 17], tetrahedra and octahedra [18] and hexagonally shaped islands [19]. Energetic ground states of spherical core-shell structures have been

studied analytically by deriving expressions for the micromagnetic energy contributions [20].

This paper on the study of the magnetic behaviour of soft-magnetic core-shell pyramids is structured as follows. In section 2, we briefly discuss the research on core-shell structures and give a summary of corresponding experimental work on the growth of pyramidal core-shell structures. In section 3, we define the geometry (3.1), introduce the model and details of how it is implemented (3.2) and explain how the micromagnetic configurations have been computed over the parameter space of this study (3.3). The numerical results are presented in section 4. It contains an analysis of the magnetic behaviour of the core-shell structures in the absence of an external magnetic field (4.1). Characterizations of all the found remanent configurations (4.1.1 and 4.1.2) are given. A phase diagram, which delineates the energetic ground states as a function of the geometry-defining parameters, is presented and discussed (4.1.3), and the occurrence of an asymmetric vortex state is analysed (4.1.4). The second part of section 4 contains an investigation of the reversal behaviour along selected directions of the applied fields (4.2). Finally, we summarise our findings in section 5.

2. Motivation

As discussed in the introduction, most experimental and theoretical research has been devoted to the study of simple geometries such as circular or square platelets. This is mainly due to practical difficulties that arise in the growth of more complex geometries. In the context of 3D objects, core-shell structures are advantageous for the following reasons: they reduce the amount of magnetic material used compared to filled 3D objects, which, in the case of expensive components, may lead to significant cost reductions. In addition, the interaction between the core and shell regions may lead to interesting physical phenomena. For example, the core region could consist of a material that is superconducting below a certain critical field, H_C. In this case, the core can exhibit re-entrant superconductivity when the applied magnetic field compensates for the stray fields due to the ferromagnetic shell. Furthermore, superconductivity can exist up to applied fields well above the bulk critical field of the core due to these effects. On the other hand, if the core material is non-magnetic (e.g. the magnetic field in the core region lies above H_C), then the magnetic behaviour of the core-shell structure will be solely governed by the ferromagnetic shell (the situation assumed in this paper). The transition between the two magnetic states of the core-shell structure depends on the properties of both core and shell materials, and on the geometry of the structure.

The work presented here only considers the properties of the ferromagnetic shell. It has been motivated by corresponding experimental work on the electrochemical growth of pyramidal core-shell structures with a silver (Ag) core and a nickel (Ni) shell ([21], figure 1), which we will briefly describe in the following: for this a two-step dual bath method is used. First, single crystalline, pyramidal-shaped silver mesostructures are deposited on a highly ordered pyrolytic graphite (HOPG) working electrode from an

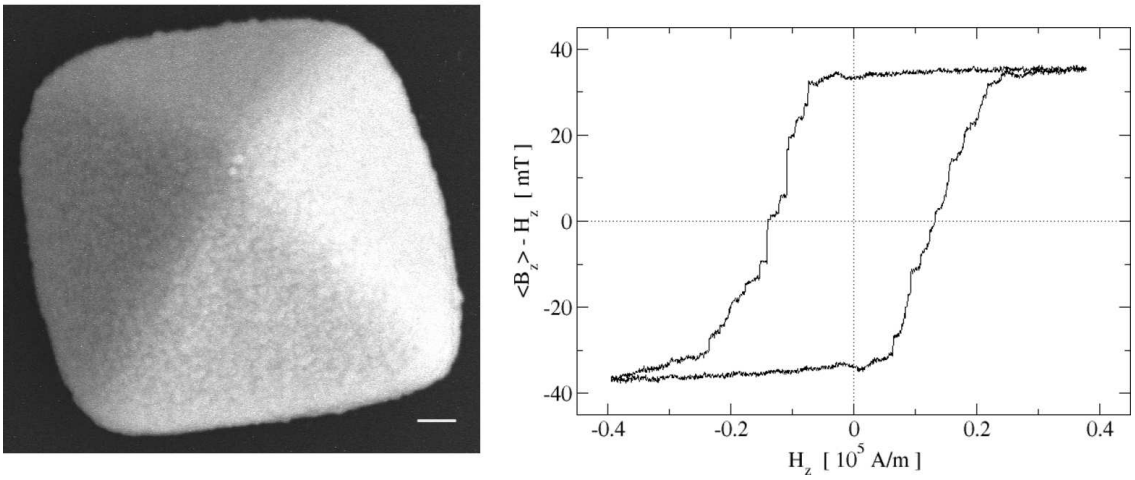

Figure 1: Left: atomic force microscope (AFM) image of a pyramidal core-shell structure with a silver core and a nickel shell. Surface roughening indicates the polycrystalline character of the nickel shell [21]. The scale bar length is 1 μm. Right: hysteresis measurement on a pyramidal Ag/Ni core-shell structure. These measurements have been carried out at 5 K using a linear array of 2 μm x 2 μm GaAs/AlGaAs heterostructure Hall probes. An individual structure has been taken from the electrode and then placed onto an active Hall probe element with its basal plane facing down. The homogeneous magnetic field has been applied perpendicular to the Hall element, a direction that we identify with the z-direction. The x-axis shows the strength of the applied magnetic field, while the y-axis depicts the magnetic field detected by the Hall element $\langle B_z \rangle$ minus the applied field H_z. The latter quantity corresponds to the stray field generated by the pyramidal shell, which is spatially averaged over the active area of the Hall element.

aqueous solution of 100 mM $AgNO_3$ at a pH value between 2 and 2.5. In the process the potential of the HOPG working electrode is first set to 1 V for 60 s, then to 0 V for 10 s and finally to -10 mV for 30 s. The silver deposition occurs during the last stage via the so-called Volmer-Weber mechanism, in which 3D nuclei are promptly formed. In the second step the electrolyte is replaced by an aqueous solution containing 2.3 M $NiSO_4$, 0.6 M $NiCl_2$ and 0.5 M boric acid. The nickel is then electrodeposited at a potential of -800 mV versus an Ag/AgCl reference electrode and a pH value of 2. Cyclic voltammograms suggest that at this potential nickel is only deposited on the metallic silver islands and not elsewhere on the HOPG electrode. A direct deposition of nickel onto HOPG turns out to be impracticable as it tends to plate rather than to exhibit a 3D growth mode. The pyramidal core-shell structures grown with this method (figure 1) have typically a base side length of 10 μm, a height of 5 μm and a shell thickness of about 100 nm.

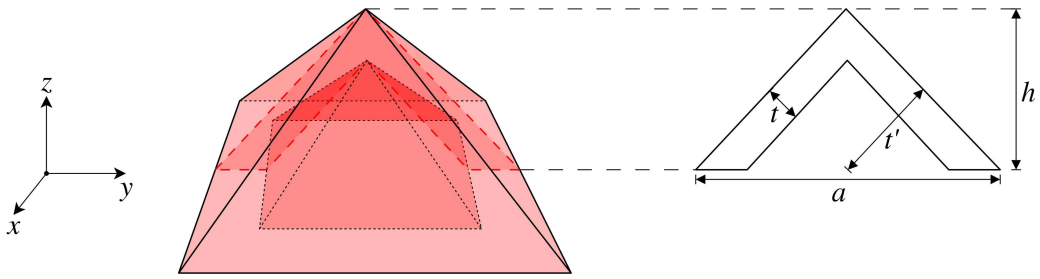

Figure 2: Sketch of a pyramidal shell structure. The left part of the figure shows a three dimensional visualization. On the right, parameters defining the shell geometry are introduced on the basis of a cross-section through the shell structure's centre. The parameter h is the height of the pyramid, a denotes its edge length and t is the thickness of the shell. t' defines the distance between each outer side face and the centre of the basal plane. Throughout the paper, we define the z-direction as the direction that is represented by the tip, while x and y are aligned parallel to the edges of the basal plane.

3. Methodology

3.1. The investigated system

We focus our micromagnetic studies on pyramidal shells with a square base. The base of the pyramid is not covered with a ferromagnetic layer as it is sitting face down on the growth substrate (i.e. the HOPG) during electrodeposition. Figure 2 shows how such a structure can be defined in terms of three parameters. The pyramidal shape is defined by the edge length a and the height h, while the parameter t is the shell thickness.

In order to limit the number of simulations for this study to a reasonable extent, we have restricted our parameter space by setting $h = a/2$, which also appears to concur with the shape of the experimentally grown structures (see section 2). Furthermore, we replace the shell thickness t in absolute units by t_{rel}, which is defined as

$$t_{\mathrm{rel}} = 100.0 \cdot \frac{t}{t'}.$$

Here, $t' = a/(2 \cdot \sqrt{2})$ is the distance of one of the triangular faces of the shell's outside to the centre of the base. t_{rel} ranges between 0.0 and 100.0, with 0.0 being the limit of an infinitely thin shell, and 100.0 representing a completely filled pyramid. Two shells with the same value for t_{rel}, say (a_1, t_{rel}) and (a_2, t_{rel}), are mathematically similar, i.e. the former can be obtained from the latter by rescaling it by a factor a_1/a_2. Thus, a may be regarded as a size parameter and t_{rel} as a shape parameter.

3.2. The micromagnetic method

The micromagnetic model, as introduced by Brown, approaches ferromagnetism on a mesoscopic scale, i.e. it only indirectly accounts for the underlying atomic structure

of the material and assumes a continuous magnetization $\vec{M}(\vec{r})$, which determines the state of the ferromagnetic structure. At each point $\vec{r}$, usually four different torques are considered to act upon $\vec{M}(\vec{r})$. These torques are due to local magnetocrystalline anisotropy, short-range exchange interaction, long-range magnetostatic interaction and an externally applied magnetic field. The former three contributions are material dependent, so that the model requires the input of corresponding parameters. These parameters are the exchange constant A, anisotropy constants of different order (K_1, K_2, ...), and the saturation magnetization M_S. Since nickel is a very promising ferromagnetic material for the growth by electrodeposition, we use the corresponding values $A = 7.2 \times 10^{-12}\,\mathrm{J\,m^{-1}}$ and $M_\mathrm{S} = 493380\,\mathrm{A}\,mathrmm^{-1}$ [22], while we neglect its highly temperature-dependent cubic anisotropy. At room temperature the anisotropy constants are $K_1 = -4500\,\mathrm{J\,m^{-3}}$ and $K_2 = -2500\,\mathrm{J\,m^{-3}}$, which are small compared to the typical magnitude of the magnetostatic self-energy $K_d = \frac{\mu_0}{2} \cdot M_\mathrm{S}^2 = 152948\,\frac{\mathrm{J}}{\mathrm{m^3}}$. Earlier studies suggest that the omission of the anisotropy term does not qualitatively alter the results within the regime investigated here (i.e. dimensions of about $60 \cdot l_\mathrm{exch}$ and below, where l_exch is the exchange length defined by $l_\mathrm{exch} = \sqrt{A/K_D}$) [12]. Furthermore, due to the polycrystalline structure of the electrodeposited nickel shell, an inclusion of magnetocrystalline anisotropy is not straightforward. We do not consider surface anisotropy, which becomes especially important for very thin shells [6], and additional energy contributions that, for example, may arise from magnetoelastic effects such as magnetostriction. The total energy E_tot of our system can be written as

$$E_\mathrm{tot} = E_\mathrm{exch} + E_\mathrm{demag} + E_\mathrm{ext}. \tag{1}$$

In order to find a configuration $\vec{M}(\vec{r})$ that minimizes E_tot, we use the Landau-Lifshitz-Gilbert (LLG) equation

$$\frac{\partial \vec{M}}{\partial t} = -\frac{\gamma}{1+\alpha^2}\vec{M} \times \vec{H}_\mathrm{eff} + \frac{\alpha\gamma}{(1+\alpha^2)M_\mathrm{S}}\vec{M} \times \left(\vec{M} \times \vec{H}_\mathrm{eff}\right), \tag{2}$$

where the effective magnetic field $\vec{H}_\mathrm{eff}$ is the variational derivative of E_tot with respect to the magnetization $\vec{M}(\vec{r})$ and accordingly has contributions stemming from the exchange and magnetostatic interactions and the external field $\vec{H}_\mathrm{ext}$, i.e.

$$\vec{H}_\mathrm{eff} = \vec{H}_\mathrm{exch} + \vec{H}_\mathrm{demag} + \vec{H}_\mathrm{ext} = -\frac{1}{\mu_B}\frac{\delta E_\mathrm{tot}}{\delta \vec{M}}. \tag{3}$$

The constant $\gamma = 2.214 \cdot 10^5\ \mathrm{m\,(As)^{-1}}$ is the gyromagnetic ratio of an electron, and α the dimensionless Gilbert damping constant. Since we are only interested in finding energy-minimizing configurations of the system, and not in the dynamics of $\vec{M}(\vec{r})$, we choose $\alpha = 1$ in order to achieve a maximal damping [22]. Equation (2) implies that the magnitude of the magnetization does not change over time, i.e. $|\vec{M}(\vec{r},t)| = |\vec{M}(\vec{r})| = M_\mathrm{S}$. Therefore, we introduce a reduced vector field $\vec{m}(\vec{r},t) = \vec{M}(\vec{r},t)/M_\mathrm{S}$ whose magnitude is 1, and use $\vec{m}(\vec{r})$ for illustrations of the magnetization in this paper. For the numerical solution of the LLG equation, we employ the micromagnetic FE simulation package Nmag [23], which discretizes the relevant fields

on a tetrahedral (i.e. unstructured) mesh and thus allows for modelling arbitrarily shaped, ferromagnetic structures. While the contributions of the exchange and the external field are obtained by a direct FE discretization of the corresponding energy terms, the hybrid FE method/boundary element method (hybrid FEM/BEM) is used to calculate the numerically expensive, magnetostatic contribution [24]. Like a direct discretization of the magnetostatic energy the latter method only requires the meshing of the ferromagnetic region $\mathcal{R}_m$, while the scaling behaviour improves from $O(N^2)$ to $O(N_S^2)$, where N and N_S denote the total numbers of nodes within $\mathcal{R}_m$ and on the surface of $\mathcal{R}_m$, respectively. We use hierarchical matrices [25] in order to approximate a dense boundary element matrix which occurs within the scheme of the hybrid FEM/BEM. This further improves the computational complexity of the method to $O(N)$. The hierarchical matrix approximations are assembled using the HCA II algorithm [26] with a set of parameters as given in [27]. We find that the use of hierarchical matrices works well for the studied pyramidal geometries, as the error introduced by this approximation is small compared to other numerical errors in the computation of $\vec{H}_{\mathrm{demag}}$, which are driven by the discretization (see discussion of tetrahedra edge length below). Each tetrahedral mesh has been created with the commercial software tool Fluent Gambit 2.4.6. When creating the unstructured mesh its resolution has to be such that the computation of the model's exchange and magnetostatic fields is reasonably accurate. For a sufficient accuracy in the exchange field computation the edge lengths of all tetrahedrons should typically lie below the exchange length l_{exch} [18, 28], which in the case of nickel is equal to 6.86 nm. Since Gambit does not provide a parameter for specifying a maximal edge length, we use an h-type refinement [29], i.e. add a nodal point to the centre of tetrahedron edges a with $|a| > l_{\mathrm{exch}}$ and rearrange adjacent tetrahedra accordingly, in order to ensure a resolution below l_{exch}. For each simulation we have checked whether the maximal angle between the magnetic moments of adjacent mesh nodes (the so-called spin angle) of the relaxed configuration is about 30° or below. Spin angles, which dramatically exceed this limit, underestimate the contribution of the local exchange field and may lead to incorrect results [30]. In order to estimate the error in the computation of the magnetostatic field $\vec{H}_{\mathrm{demag}}$, we have systematically varied the mesh resolution to compute $\vec{H}_{\mathrm{demag}}$, and repeated this procedure for different edge lengths a, shell thicknesses t_{rel} and magnetization configurations. As an estimate for the error we have used the average of $\vec{H}_{\mathrm{demag}}$over all mesh nodes (in a more rigorous analysis one should use a norm as defined in [31]), and demand that its variation as a function of the mesh resolution should lie well below 1 % (in line with [31]). Our findings are that the edge lengths of the tetrahedra should be below the values $0.035\,a$ or $0.5\,t$, where a and t are the base length of the pyramidal structure and the shell thickness, respectively (see geometry figure 2 for a and t). In summary, depending on the size and shape of the pyramidal shell geometry we have chosen the smallest of three threshold values (exchange length, $0.5\,t$, $0.035\,a$), to obtain satisfactory accuracy. For the time integration of (2), Nmag uses an implicit time integration scheme as reported in [32] and made available in the Sundials software library [33]. The system is integrated until

the angular rate of change of the magnetization is below $1^\circ\, mathrmns^{-1}$ at every mesh node.

3.3. Exploring the parameter space

The parameters a and t_{rel}, as introduced in section 3.1, define a 2D phase space. One goal of this paper is to examine this phase space for micromagnetic ground state configurations in the absence of an externally applied magnetic field. Ground state configurations minimize the micromagnetic energy of (1). We start these investigations by relaxing the magnetization for different parameter sets (a, t_{rel}) and initial configurations. The edge length a is set to values at 20, 50, 100, 150, 200, 250, 300, 350 and 400 nm (i.e varied between $a_{\mathrm{min}} \approx 3 \cdot l_{\mathrm{exch}}$ and $a_{\mathrm{max}} \approx 60 \cdot l_{\mathrm{exch}}$), while thicknesses of $t_{\mathrm{rel}} = 5$, 10, 15, 20, 30, 40, 50, 60, 70, 80, 90 and 100% are used. As initial configurations we choose different homogeneously aligned magnetizations pointing in directions such as $(1, 0, 0), (0, 0, 1), (1, 1, 0)$ and $(1, 1, 0.5)$ (with respect to the coordinate system defined in figure 2). Obtaining a set of stable configurations for each investigated point (a, t_{rel}) we assume the configuration with the lowest micromagnetic energy to be the ground state. The corresponding results are then most conveniently summarized in a phase diagram which states the micromagnetic ground state as a function of a and t_{rel}.

In order to add phase boundaries to the phase diagram, we use a technique similar to the one described in [34]. We start from the relaxed micromagnetic configuration and rescale the mesh such that the edge length a increases or decreases by Δa, i.e. the rescale factor is $(a + \Delta a)/a$ or $(a - \Delta a)/a$, respectively. One should note that the described procedure does not work with a variation of the shape parameter t_{rel}. We extrapolate the rescaled micromagnetic configuration to a new mesh that discretizes the geometry of the new size (otherwise the rescaling procedure would change the resolution of the mesh) and relax the system to a new stable state. Usually the system will relax quickly, since we already start from a very good approximation of the domain structure. However, if the domain structure becomes unstable at the new system size, it will collapse to a qualitatively different micromagnetic configuration. We use this procedure iteratively, when the ground state configuration between adjacent points of the same thickness t_{rel} changes. Starting from a configuration corresponding to a small value of a and gradually increasing a, we get a curve for the total energy as a function of a. Starting from a (different) configuration corresponding to a large a and then decreasing a, we obtain another data set of the total energy as a function of the edge length a. Subsequently, we determine by a low-order polynomial interpolation the point a_{trans} at which the energies of both configurations cross over. When both states decay spontaneously into each other we choose a_{trans} as the arithmetic mean value of the two edge lengths between which the transition occurs. Repeating this procedure for different thicknesses t_{rel} one can draw phase boundaries between areas of different micromagnetic ground states. Depending on the magnitude of a, we use different values for Δa. We

choose $\Delta a = 2\,\mathrm{nm}$ for $10\,\mathrm{nm} < a < 20\,\mathrm{nm}$, $\Delta a = 5\,\mathrm{nm}$ for $20\,\mathrm{nm} < a < 50\,\mathrm{nm}$ and $\Delta a = 10\,\mathrm{nm}$ for $50\,\mathrm{nm} < a < 400\,\mathrm{nm}$.

A problem in our approach may arise because the primary data points of the phase diagram have been obtained from a finite set of initial states. Thus, it could happen that at a certain parameter point (a, t_{rel}) a magnetization configuration may not have been found although it may be stable or even the ground state.

4. Numerical results

4.1. Energetic ground states at $H_{\mathrm{ext}} = 0$

In this section, we present results on the micromagnetic states of pyramidal shells (see section 3.1) in the absence of an external magnetic field. In accordance with previous work on soft magnetic structures [12, 18], we find that in the investigated regime two types of ferromagnetic domains occur: the so-called single domain (or quasi-homogeneous) states and vortex states.

4.1.1. Single-domain states Single-domain states are quasi-homogeneous and have a well-defined mean magnetization direction. They usually occur in the limit of very small structures (at dimensions of just a few exchange lengths). While the exchange interaction leads to the quasi-homogeneity, magnetostatic effects govern the direction of the mean magnetization. In the literature, one distinguishes between two types of anisotropies arising from the magnetostatic contribution to the micromagnetic energy functional (1). Shape anisotropy describes the anisotropy of a completely aligned magnetization due to the shape of the ferromagnet. However, the deviations from homogeneous alignment may lead to a change in the character of the anisotropy, i.e. the assumption of homogeneous magnetization becomes invalid. This interaction between an inhomogeneous magnetization and the shape is called configurational anisotropy. The name derives from the fact that an inhomogeneous state generally changes with the direction in space, and the anisotropy follows from the different energies of those configurations. Configurational anisotropy is usually studied for quasi-homogeneous states [5, 18], while an analysis for more complex states (e.g. vortex states) turns out to be problematic [18]. We have investigated the shape anisotropy of our structures by systematically varying the spatial orientation of the homogeneous magnetization and computing the corresponding mean magnetostatic energy density. As a result, we have found that the shape anisotropy has a uniaxial symmetry with the structure's basal plane being the easy plane. However, it turns out that due to configurational anisotropy quasi-homogeneous states, whose mean magnetization aligns either along the x (or y) direction (as defined in figure 2) or the diagonal of the basal plane, are energetically favoured. Figure 3 shows the observed single-domain states. Every state (apart from the state of figure 3c) corresponds to a state observed in square nanostructures [5, 6], i.e. shows a similar symmetry. However, the states of the pyramidal system are more

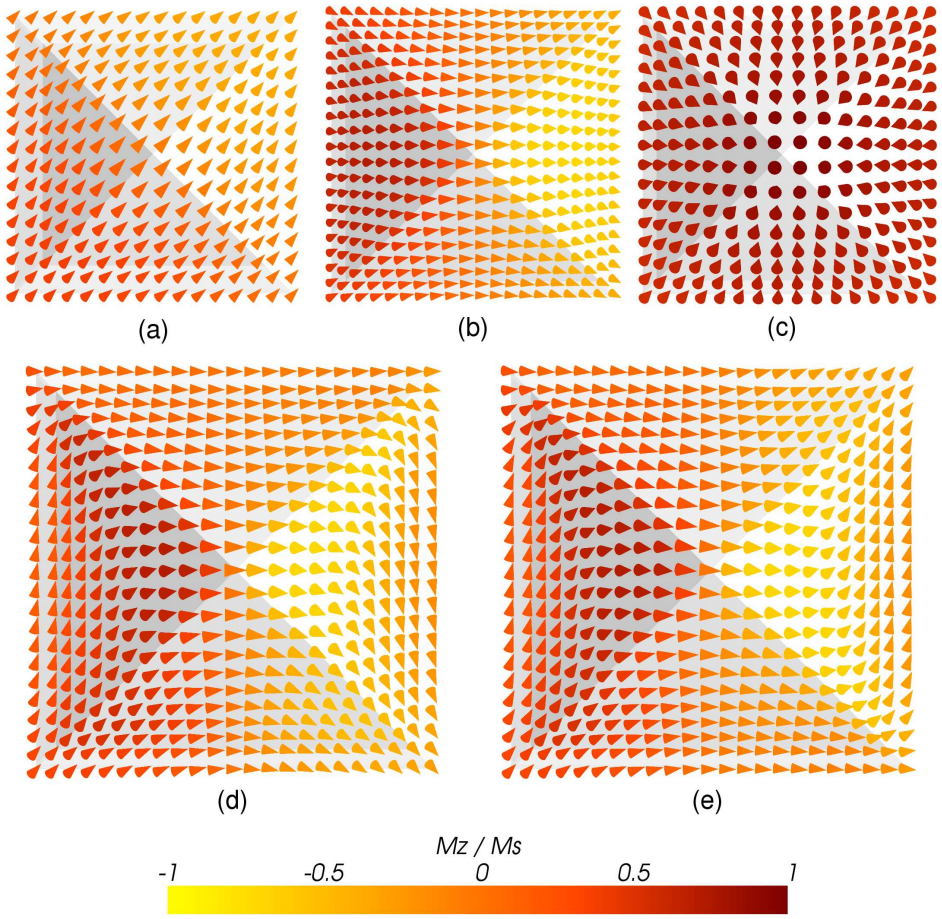

Figure 3: Top view (in negative z-direction) of stable single domain states. The observed states are (a) an onion state, (b) a flower state, (c) a single-domain state aligned along the z-direction, (d) a C state, and (e) an S state. The pyramidal geometries correspond to the following parameter sets: $a = 35\,\mathrm{nm}$ and $t_{\mathrm{rel}} = 20\,\%$ for the onion state, $a = 120\,\mathrm{nm}$ and $t_{\mathrm{rel}} = 10\,\%$ for the flower state, $a = 60\,\mathrm{nm}$ and $t_{\mathrm{rel}} = 10\,\%$ for the single-domain state in figure (c), and $a = 300\,\mathrm{nm}$, and $t_{\mathrm{rel}} = 10\,\%$ for the C and the S state. For illustration purposes a semi-transparent depiction of the pyramidal shells has been overlaid onto each picture.

inhomogeneous in the sense that there is a significant variation of the magnetization's z-component. This is due to the fact that the magnetization tries to avoid surface charges on the inner and outer side faces of the shell by aligning parallel to those faces.

We refer to the single-domain state, whose mean magnetization is aligned along the diagonal of the basal plane as an onion state (sometimes also called the leaf state). Figure 3a shows the magnetization of the onion state on the outer surface of a pyramidal shell with ($a = 35\,\mathrm{nm}$, $t_{\mathrm{rel}} = 20\,\%$). Moving from the lower left to the upper right corner the magnetization tries to follow the surface geometry by pointing upwards on the lower left and pointing downwards on the upper right half. Due to the symmetry of this state the z-component of the magnetization is zero across the crest, around which the

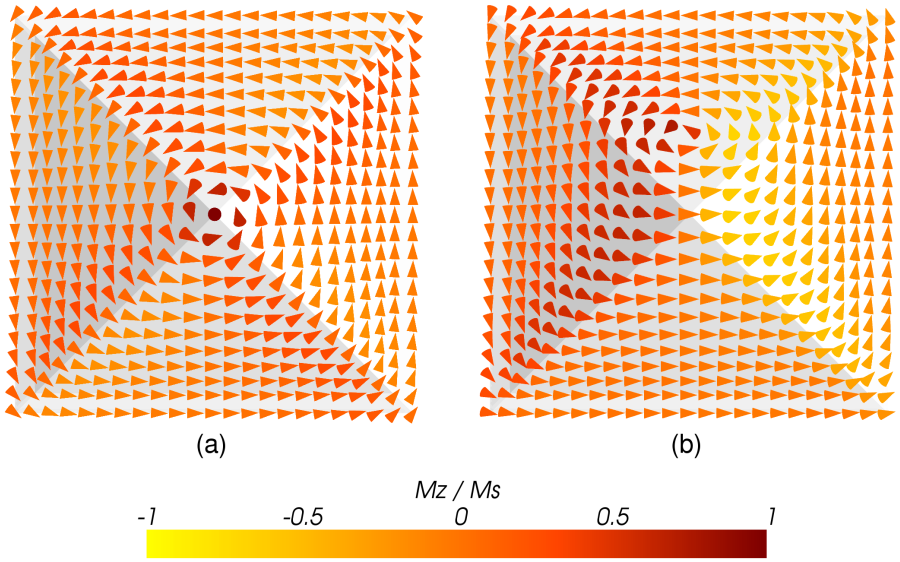

Figure 4: Top view (in negative z-direction) of stable vortex states. We observe a symmetric vortex state (a) and an asymmetric vortex state (b). The pyramidal structure has an edge length of $a = 300\,\mathrm{nm}$ and a thickness of $t_{\mathrm{rel}} = 10\,\%$.

proximity of negative and positive surface charges leads to a high magnetostatic energy density. The latter effect is inherent to the onion state.

The state of figure 3b is called a flower state. It features the typical tilting in the vicinity of corners, which gives a flower-like impression. We observe that the spatially averaged magnetization, which is aligned with either the x- or y-axis, increases with growing shell thickness. This is due to surface charges that can be created on the basal plane of the pyramidal shell. The area of the latter grows with increasing shell thickness. Thus, the higher impact of the basal plane leads to generally better alignment of the magnetization along the x (or y) axis for thick shells.

Figure 3d shows a so-called buckle or C state. The latter name derives from the shape of the flux lines, which, in the perspective of figure 3d, resembles the letter C rotated 90° in the clockwise direction. Compared to a flower state, a C state reduces the magnetostatic energy by a higher degree of flux closure. This happens at the expense of a higher exchange energy.

The so-called S state is shown in figure 3e. Analogous to the C state, it gets its name from the shape of the flux lines that follow the shape of the letter S. Compared to the flower and the C state the mean magnetization of the S state is shifted towards a diagonal of the basal plane, i.e. from $(1, 0, 0)$ to typically about $(0.75, 0.25, 0)$.

Figure 3c shows a quasi-homogeneous metastable state found for very thin pyramid shells with a mean magnetization pointing in the z-direction. As this state is only metastable for very thin and small structures ($a \gtrsim 100\,\mathrm{nm}$, $t_{\mathrm{rel}} \gtrsim 10\%$) but unstable otherwise, we will not discuss it in what follows.

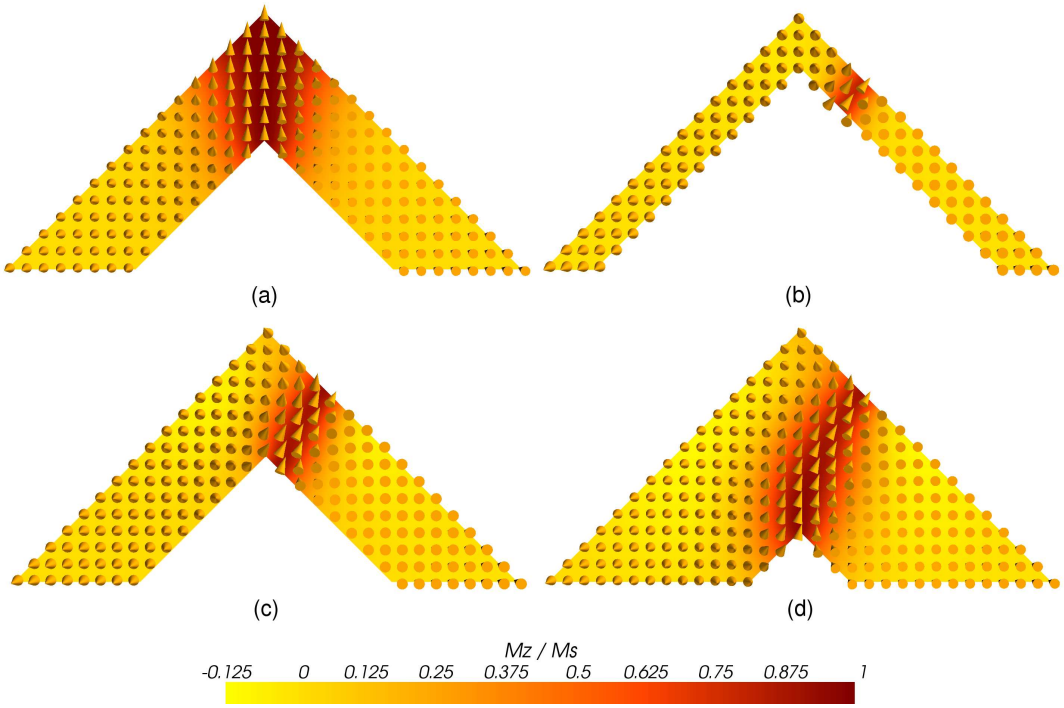

Figure 5: (a) Cross-sectional display of the symmetric vortex state. The pyramid in this example has an edge length of $a = 150\,\text{nm}$ and a thickness of $t_{\text{rel}} = 50\%$. (b-d) Cross-section through an asymmetric vortex state for an edge length of $a = 300\,\text{nm}$ and three different thicknesses t_{rel}: 20 % (b), 50 % (c) and 80 % (d). The cross-sectional plane centrally cuts the pyramidal structure in all depicted images.

4.1.2. Vortex states There is no mathematically rigorous definition of a vortex state in micromagnetics [35]. For thin films a vortex state consists of a small, out-of-plane vortex core and an in-plane magnetization curling around the core. The in-plane magnetization helps form closed flux lines, i.e. reduces surface charges, at the expense of a higher exchange energy in the region around the vortex core. However, the magnetostatic energy of the vortex core cannot be neglected [6, 7]. For our geometries we observe two different vortex states (figure 4).

Figure 4a shows a vortex state with a core aligned along the direction of the pyramid's tip (i.e. in the z-direction). Due to the core position in the symmetry centre of the geometry, we will refer to this state as the symmetric vortex state. We note two features: firstly, the z-component of the curling magnetization fluctuates around the edges between two adjacent side faces. This effect is just visible in the form of colour variations in figure 4a but more pronounced in the warp plane representation of figure 9 (top image). Secondly, the vortex core broadens towards the top of the pyramid (see figure 5a). A consequence of this broadening is a decrease in the exchange energy density within the vortex core towards the top of the pyramid.

Figure 4b shows the asymmetric vortex state whose core is sitting on one of the four (outer) side faces of the shell. A characteristic of the asymmetric vortex state is

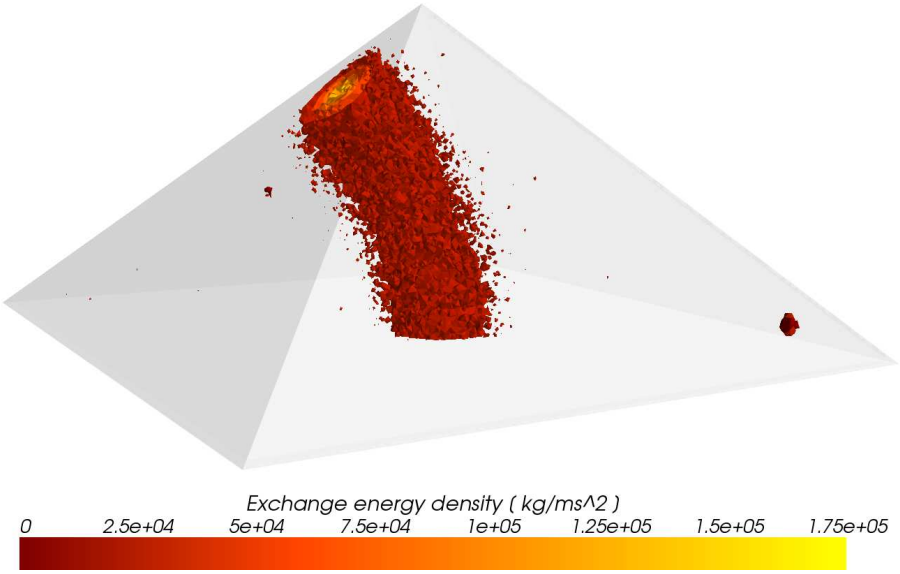

Figure 6: Equipotential surfaces of the exchange energy density displaying a vortex state with a bent vortex core. The geometry is a full pyramid with a basal plane edge length of 300 nm and a height of 150 nm. The exchange energy density is defined as $u_{\mathrm{exch}} = \vec{M}\cdot\vec{H}_{\mathrm{exch}} = 2A\,\vec{m}\cdot\nabla^2\vec{m}$. Artifacts from the numerical calculation of the exchange energy appear to lead to non-smooth surfaces.

that its remanent magnetization is not only carried by the vortex core but also has a component parallel to the basal plane. This can be seen in figure 4b where more "magnetic moments" point to the right than to the left. We discuss in section 4.2 that this leads to an interesting magnetic reversal behaviour. Figure 5 shows that the character of the state changes with varying shell thickness. While for thin shells ($t_{\mathrm{rel}} \lesssim 50\,\%$) the vortex core runs from the outer face straight to the corresponding inner face (see figures 5b and c), it tends to bend towards the tip of the structure's core for larger values of t_{rel} (figure 5d). This vortex core bending is also illustrated in figure 6 for a conventional pyramid, i.e. t_{rel} equals 100 %. The position of the vortex on the outer side face lies in the vicinity of the pyramid tip for most values of t_{rel}, but is shifted towards the centre of the triangular face for very thin shells below 10 %.

4.1.3. Phase diagram and metastability The phase diagram of figure 7 summarizes which state minimizes the total micromagnetic energy, i.e. is the ground state, for which geometry (defined by the parameter set (a,t_{rel})). Physically the ground state can be interpreted as the state which should be formed when a ferromagnetic structure is slowly cooled below its Curie temperature to 0 K [36]. According to [36], in the limit of large thermal activation, the ground state tends to be the same as the remanence state after saturation by an applied field. However, due to the complicated energy landscape of ferromagnetic systems it is difficult to make a general remark on the tendency of systems to adopt the micromagnetic ground state. In particular, for soft magnetic

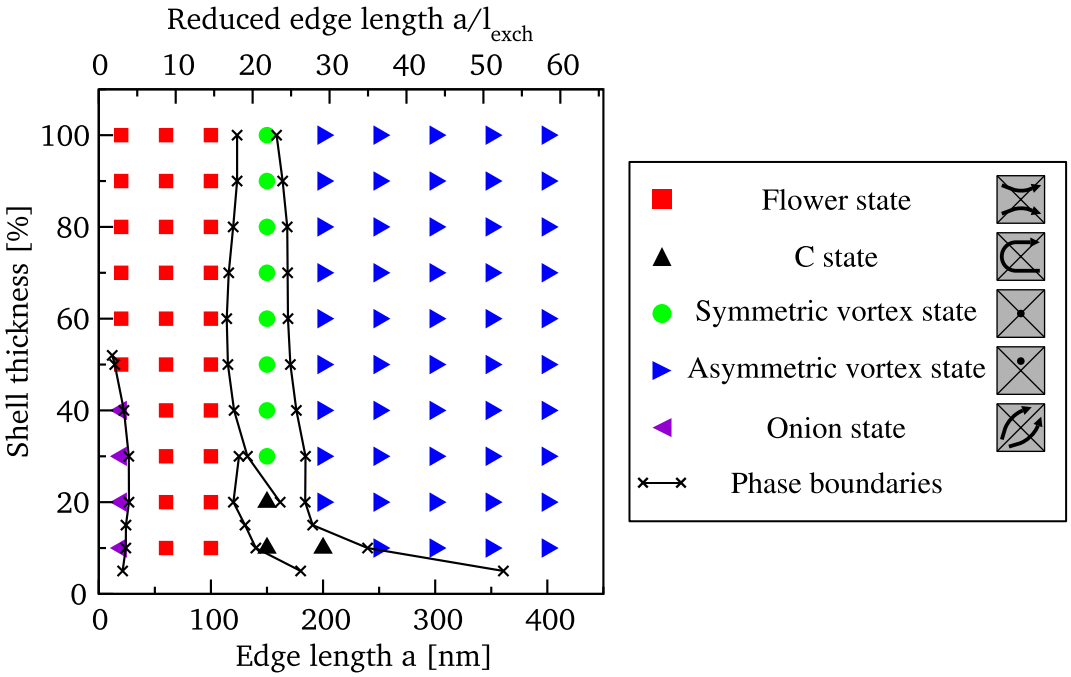

Figure 7: Phase diagram showing the ground states for different pyramidal structures. The two parameters are the edge length of the outer pyramid and the thickness of the pyramid shell. For better readability we have added schematic plots to the legend, which highlight the main features of each ground state from a top-down perspective.

structures, metastable states may occur. Therefore, we will later discuss in figure 8 the stability regimes of all domain structures, which have been observed at the shell thicknesses $t_{\mathrm{rel}} = 10\,, 50$ and $100\,\%$. One should note that our model does not consider the effects of thermal activation on the stability of different configurations.

For small structure sizes (i.e. $a < 100\,\mathrm{nm}$) only the flower and the onion state are energetic ground states. As can be seen from figure 7 the onion state minimizes the energy roughly for edge lengths a below $25\,\mathrm{nm}$ and shell thicknesses t_{rel} smaller than $55\,\%$. The simulation results do not give obvious reasons why the onion state becomes metastable at $t_{\mathrm{rel}} \lesssim 55\,\%$. However, corresponding investigations on square platelets have shown that the onion state becomes energetically favourable with respect to the flower state for larger values of the ratio between size and thickness [5, 36], which is qualitatively in agreement with our findings. These investigations have also shown that for small platelet thicknesses the onion state is the micromagnetic ground state in a wide size range. Thus, we observe a suppression of the onion state for the pyramidal structures. The reason seems to be the high magnetostatic energy density in the vicinity of the crest, which is inherent to the onion state.

At larger edge lengths a the micromagnetic ground state crucially depends on the shell thickness t_{rel}. For thicknesses t_{rel} above $30\,\%$ the symmetric vortex state becomes the ground state in a range between 120 and $180\,\mathrm{nm}$, above which the asymmetric vortex state minimizes the micromagnetic energy. Here, the edge length a_{trans} at which these

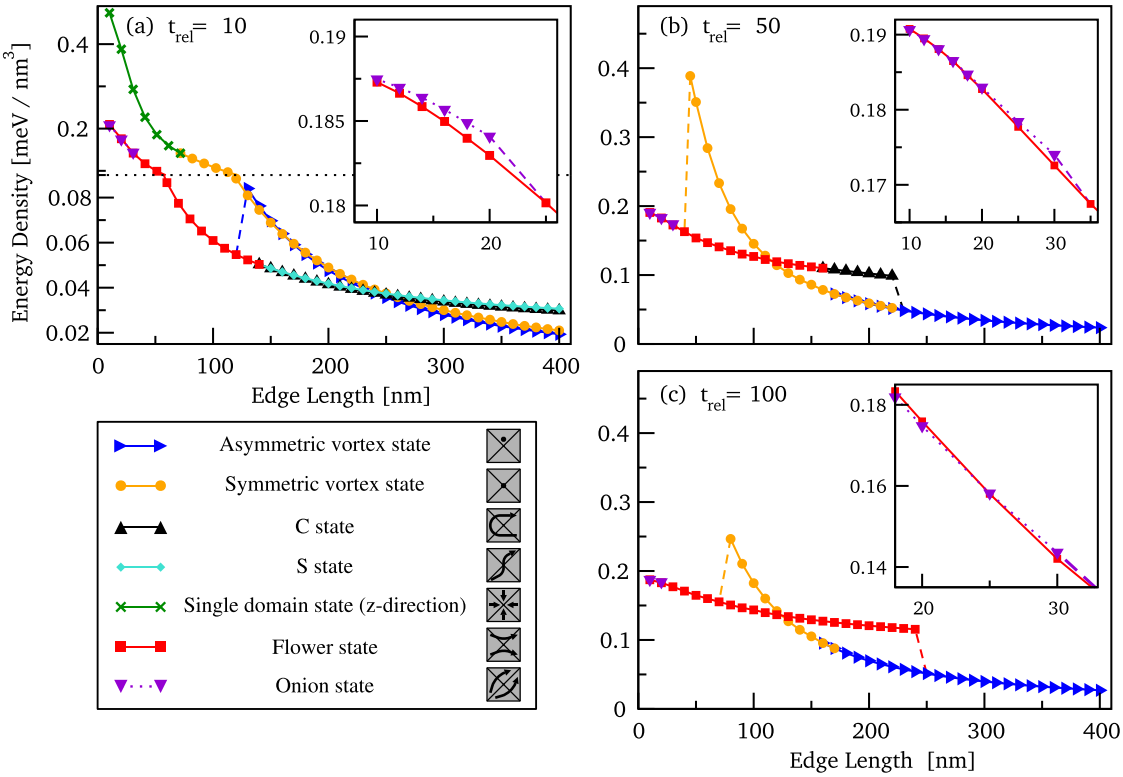

Figure 8: Dependency of the energy density of different micromagnetic configurations on the size of the shell structure. Three different thicknesses t_{rel} are considered: (a) 10%, (b) 50%, and (c) 100%. The dashed lines denote transitions between different states, i.e. the state with the higher total energy becomes unstable and the lower-energy state develops. For a better readability we added schematic plots to the legend, which highlight the main feature of each ground state from a top-down perspective.

transitions occur depends weakly on the shell thickness. Below $t_{\mathrm{rel}} = 20\,\%$ the situation is different: with increasing edge length a the lowest energy state changes from the flower state to the C state and from the C state to the asymmetric vortex state. However, in this region of the phase diagram a_{trans} strongly depends on the shell thickness t_{rel} itself. The occurrence of the C state at low values of t_{rel} can be readily understood: the penalty in the magnetostatic energy for the C state decreases with decreasing t_{rel}, as fewer surface charges on the basal plane are created.

Another feature of very thin shells is a growth in the number of metastable states (figure 8). The number of stable configurations (i.e. curves in figure 8) is 7 for $t_{\mathrm{rel}} = 10\,\%$, 5 for $t_{\mathrm{rel}} = 50\,\%$ and 4 for $t_{\mathrm{rel}} = 100\,\%$. Furthermore, the stability range of the quasi-homogeneous states (C and S states) and the symmetric vortex state extends to $a_{\mathrm{max}} = 400\,\mathrm{nm}$ for $t_{\mathrm{rel}} = 10\,\%$, while for $t_{\mathrm{rel}} = 50\,\%$ and $t_{\mathrm{rel}} = 100\,\%$, only the asymmetric vortex state is stable at large a. Thus the energy landscape becomes more complex, i.e. it contains more local minima, for very thin shells.

Figure 8 shows that the S state only occurs as a metastable state. We find that

its total micromagnetic energy is always higher than the energy of the C state, a result that also has been found for square films [6, 8]. A possible explanation is the larger distance between positive and negative surface charges for the S state [6].

4.1.4. Why does the asymmetric vortex state occur? The phase transitions from a flower state to a C state, and from a flower or C state to a vortex state (both symmetric and asymmetric), can be qualitatively explained in terms of (partial) flux closure and a corresponding reduction of the magnetostatic energy. In contrast, the physics driving the transition between the symmetric and the asymmetric vortex state is less evident and one has to take a closer look at the interplay between the geometry and the magnetization. In this section, we will qualitatively explain this transition, and thus the occurrence of the asymmetric vortex state. The fact that the asymmetric vortex state is the ground state at large sizes a suggests that it reduces the magnetostatic energy with respect to the symmetric vortex state. A key role in this reduction is played by the edges separating adjacent side faces on the outside of the shell. Figure 9 compares the magnetization, the demagnetization field, and the magnetostatic energy density of the symmetric and the asymmetric vortex states for a cross-section, which lies perpendicular to the z axis. The magnetostatic energy density is defined as

$$u_{\text{demag}} = -\frac{1}{2}\vec{M} \cdot \vec{H}_{\text{demag}}, \tag{4}$$

so that a parallel alignment of magnetization $\vec{M}(\vec{r})$ and demagnetization field $\vec{H}_{\text{demag}}$ is favoured. Let us first discuss the symmetric vortex state: Surface charges close to the edges of the outer surface, i.e. the corners of the cross-section in figure 9, create a local demagnetization field, which approximately aligns anti-parallel to the magnetization (see top left and middle left image of figure 9), corresponding to a local increase in the magnetostatic energy density. Therefore, the observed fluctuations of the magnetization around the edges of the outer side faces (see figure 9 (top)) can be understood in terms of a reduction of surface charges and a resulting lower demagnetization field. Towards the tip of the pyramid the area of the cross-section decreases and the impact of the edges becomes more significant. As a consequence the magnetization is increasingly driven out of the xy-plane so that this effect qualitatively explains the broadening of the vortex core as observed in figure 5a. Effects at the edges between the inner side faces of the shell are far weaker. This is mainly because the large demagnetization fields, which are created between the areas of positive and negative surface charges, lie in the vacuum region, and therefore do not contribute to the micromagnetic energy functional. This is illustrated in the sketch of figure 10.

When comparing the micromagnetic energy densities of an asymmetric and a symmetric vortex state (figure 9 (bottom)), a reduction of magnetostatic energy density at the edges of the outer surface can be observed for the asymmetric vortex state. It can be attributed to the significant z-component of the magnetization in the vicinity of the edges (figure 9 (top)). Firstly, this reduces surface charges and thus the magnitude of the local demagnetising field as shown by figure 9 (middle). Secondly, figure 9 (middle)

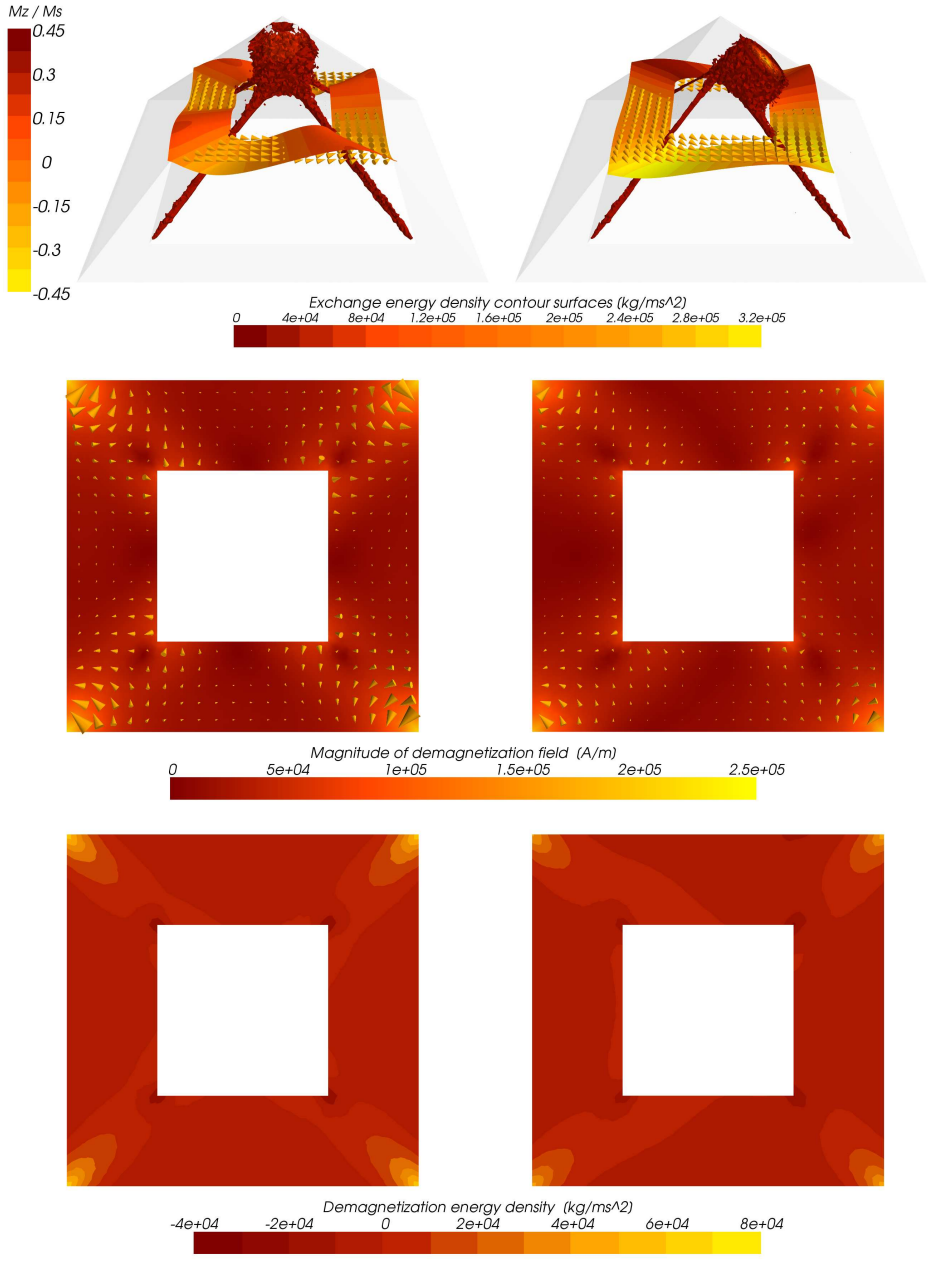

Figure 9: Different fields in a cross-sectional plane are shown for the symmetric (left) and the asymmetric (right) vortex state. The cross-section is perpendicular to the z-axis and intersects it at $z = 50\,\mathrm{nm}$ ($z = 0\,\mathrm{nm}$ corresponds to the basal plane). Within all images of the asymmetric vortex state the bent vortex core points towards the right. The geometry parameters are $a = 240\,\mathrm{nm}$ and $t_{\mathrm{rel}} = 30\%$. Top: the arrows in the plane represent the magnetization. Supplementary information is given by the warp plane, which bends out of the cross-plane. The displacement is proportional to m_z. Quantitative values of m_z can be taken from the colouration of the warp plane and the colour bar on the left. The exchange energy density of both configurations is represented in the form of contour surfaces. These reveal the location of the vortex core. Middle: demagnetization field. The arrows are scaled according to the strength of the local demagnetization field. Bottom: magnetostatic energy density.

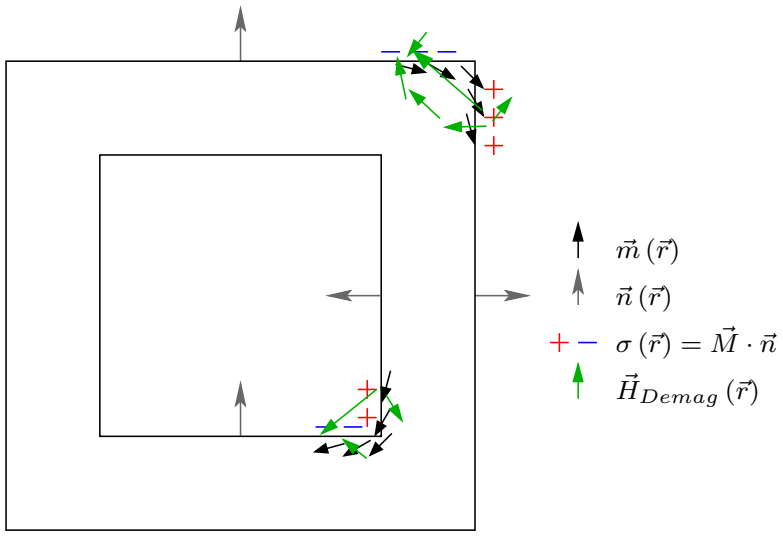

Figure 10: Cross-section of a pyramidal shell illustrating the creation of surface charges near corners on the shell's inner and outer surfaces. The symbols defined in the plot correspond to the magnetization $\vec{m}(\vec{r})$, the surface normals $\vec{n}(\vec{r})$, magnetic surface charges $\sigma(\vec{r})$, and the demagnetization field $\vec{H}_{\mathrm{demag}}$. The resulting demagnetization fields and their orientation with respect to the magnetization govern the magnetostatic energy density. The plot gives a qualitative idea of the physical behaviour, but the lengths of vectors and the number of each symbol do not rigorously mirror corresponding physical quantities.

also shows that the symmetry (i.e. the direction) of the demagnetizing field remains basically unaltered, so that magnetization and demagnetizing field subtend a smaller angle, i.e. are not anti-parallel any more. According to (4), this leads to a reduction of the magnetostatic energy density u_{demag}.

In section 4.1.2, we have discussed that the core of the symmetric vortex state broadens towards the tip of the pyramidal structure. Accordingly, figure 9 (top) shows a very low exchange energy density at the top of the pyramidal structure for the symmetric vortex state, compared to the values shown for the core of the asymmetric vortex state. The much higher exchange energy density at the tip of the inner side faces is not shown in this figure. Generally we find that the exchange and magnetostatic energy densities are higher within the displaced core. As other energetic differences (e.g. at the edges of the inner surface) are relatively small, the transition between the symmetric and the asymmetric vortex state seems to be governed by the competition between the magnetostatic energy density at the edges of the outer surface and the total micromagnetic energy density within the vortex core. More generally, we can conclude that a vortex configuration, whose core ends at a corner with converging edges, leads to high magnetostatic energy densities around the edges. This also may be an important factor in octahedra and cubes, where, for large enough structures, a vortex core aligned along a diagonal (i.e. the core ends in corners) switches to a vortex configuration with

its core aligned along face normals [18]. Also the twisted vortex state observed for cubes [12] could be driven by similar edge effects as it becomes prominent in the limit of soft materials.

4.2. Hysteresis

Although a direct observation of ferromagnetic states by a direct measurement of the magnetization is possible (for example by using magnetic force (MFM) or spin-polarized scanning tunnelling microscopy (SP-STM) [37]), hysteresis measurements are often more pertinent for a characterization of the ferromagnetic properties of a structure. This is especially true for 3D structures like the pyramidal shells studied in this paper, as the above-mentioned methods are surface techniques and only relatively straightforward to use on planar, 2D structures. From a hysteresis measurement one can obtain parameters such as the coercivity, susceptibility and the hysteresis [1], which quantify the magnetic properties. Furthermore, the knowledge of which state develops from a configuration, where the magnetization is homogeneously aligned along a certain direction in space, is essential to the research on ferromagnetic structures as it provides the opportunity to establish desired magnetic states. In the following section, we focus on the qualitative behaviour of the magnetic reversal and investigate intermediate magnetic configurations occurring between the saturated states and their effect on the hysteresis curve.

We apply and change the external magnetic field $\vec{H}_{\text{ext}}$ along one of the edges of the structure's basal plane (i.e. the x- or the y-direction in figure 2) and along the direction of the pyramid tip (z-direction). We choose the former direction since it corresponds to the system's easy axis (for reasonable large system sizes where configurational anisotropy becomes important). The latter one is a suggested direction because it is perpendicular to the bottom layer. Therefore, the external magnetic field can be aligned accordingly and corresponding hysteresis measurements are easily realizable in experiments. The reversal simulations are performed by systematically changing the external field in small steps, and relaxing the magnetization to a stable configuration after each step. For every simulation, the external field is initially set to 3.0 T. From there the field is first reduced in steps of 0.2 to 1.0 T, then in finer intervals of 0.05 to 0.2 T, and finally to zero in 0.01 T steps. Afterwards the external field is changed equivalently from zero to −3.0 T. We have performed hysteresis simulations at system sizes $a = 100\,\text{nm}$, $a = 150\,\text{nm}$ and $a = 250\,\text{nm}$ for a thin shell ($t_{\text{rel}} = 10\,\%$), a shell ($t_{\text{rel}} = 50\,\%$) and a conventional pyramid ($t_{\text{rel}} = 100\,\%$). Those parameter sets (a, t_{rel}) correspond to regimes where either the flower state, the C state or symmetric vortex state, or the asymmetric vortex state are the ground state.

Hysteresis simulations along the z-direction, which corresponds to the hard axis direction for quasi-homogeneous states, reveal two types of reversal mechanisms: Figure 11 displays the reversal for $(a = 100\,\text{nm}, t_{\text{rel}} = 10\,\%)$ and exemplifies the first type, which occurs via an onion-like configuration. The remanent state is a symmetric vortex state (figure 11b). At a magnetic field of about $-20000\,\text{Am}^{-1}$ the vortex state

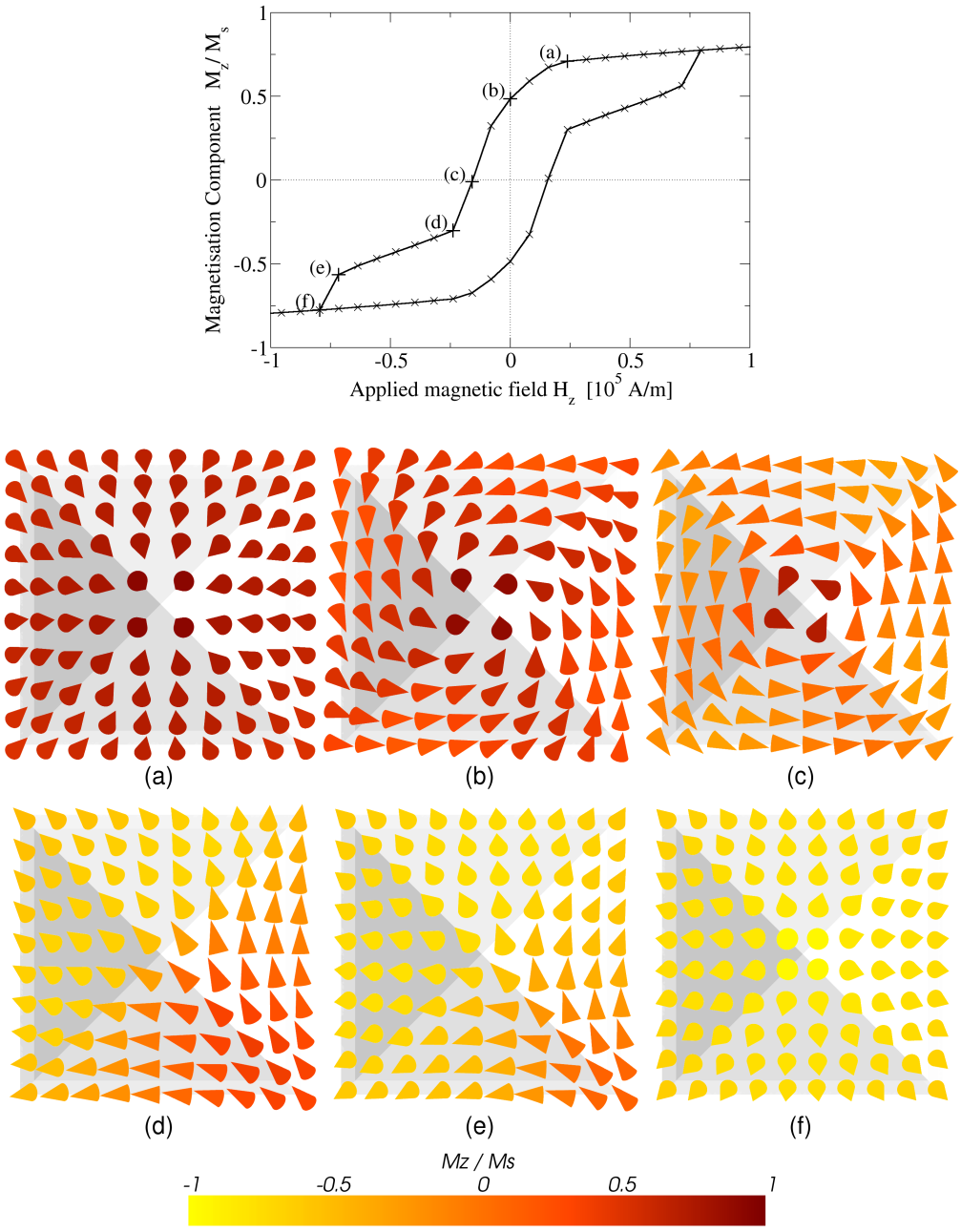

Figure 11: Hysteresis of a pyramid shell with an edge length of 100 nm and $t_{\mathrm{rel}} = 10\,\%$. The external field $\vec{H}_{\mathrm{ext}}$ is applied along the z-direction, i.e. along the direction of the pyramid's tip. For selected points (a)-(f) magnetization patterns are shown from a top-down perspective: (a) at higher external field the magnetization subsequently aligns along side faces. (b) At zero field a symmetric vortex configuration develops. (c) Magnetization partially reverses within vortex state. (d) Switch to a quasi-homogeneous state with the mean magnetization mainly aligned along a diagonal of the structure's basal plane (onion state). (e) Reversal continues within onion state. (f) Switch to state where the magnetization is aligned along side faces again.

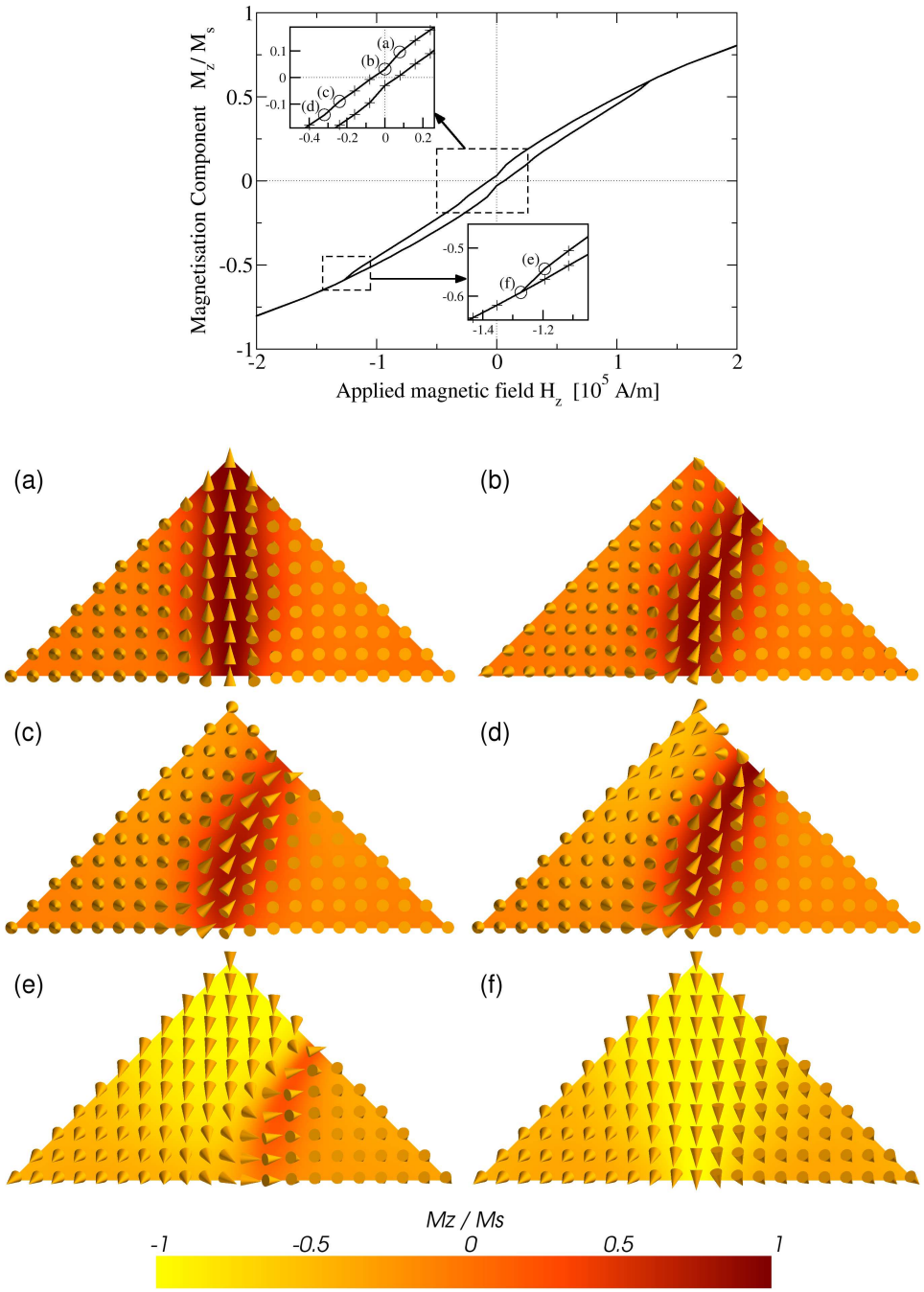

Figure 12: Hysteresis curve of a full pyramid with an edge length of 250 nm. The external field $\vec{H}_{\text{ext}}$ is applied along the z-direction, i.e. along the direction of the pyramid's tip. At selected points (a)-(f) magnetization patterns for cross-sections of the pyramid are presented. The cross-section lies in the xz-plane and intersects the pyramid centrally. (a) With decreasing external field a symmetric vortex state subsequently develops. (b) System switches to an asymmetric vortex state at remanence. (c) The asymmetric vortex state remains stable at low external fields. (d) Nucleation of what will become the core of a reversed symmetric vortex state. (e) The displaced vortex core is gradually pushed out by the developing core of the reversed symmetric vortex state. (f) Reversed symmetric vortex configuration after the displaced vortex core has been annihilated.

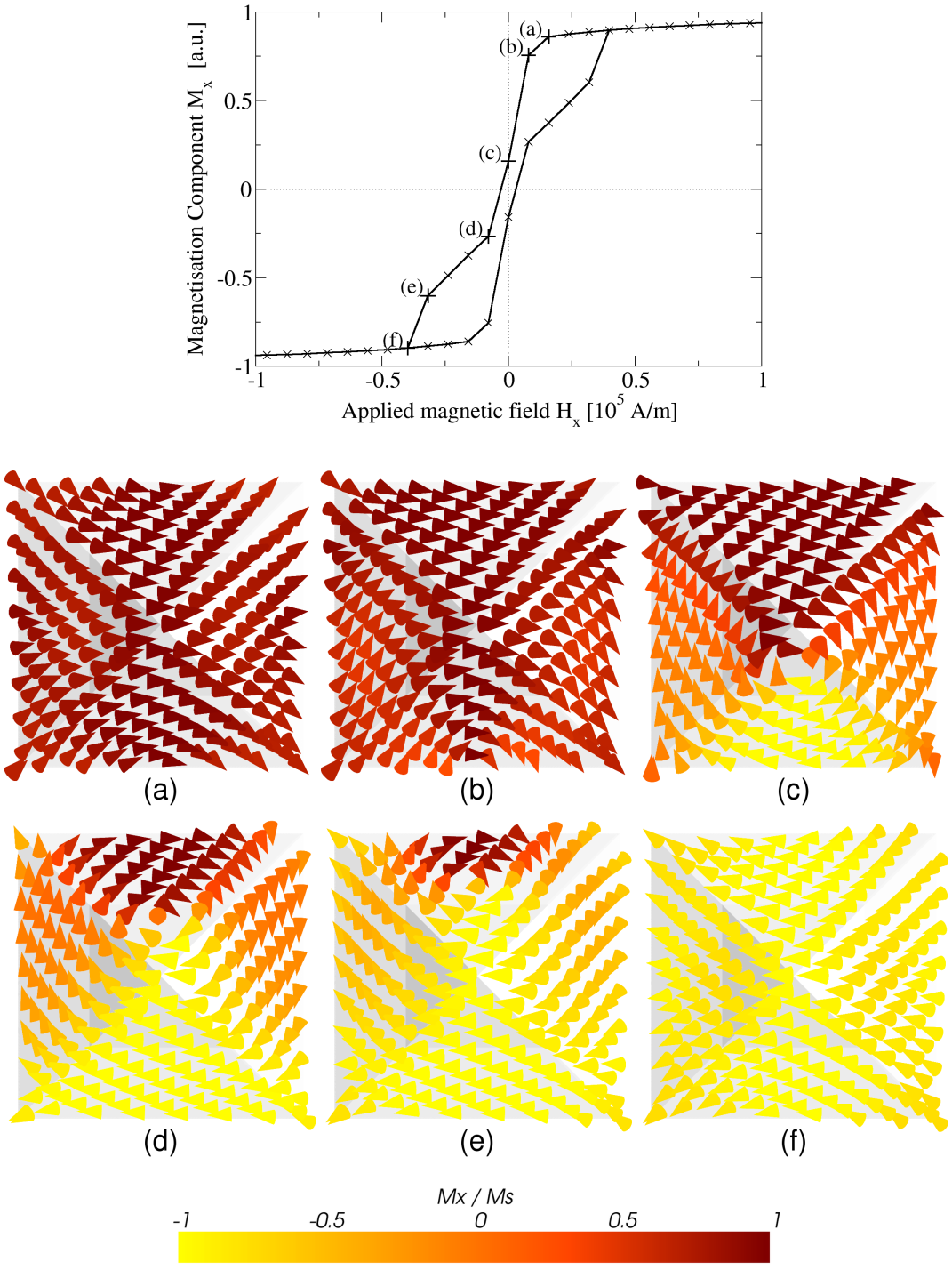

Figure 13: Hysteresis of a pyramid shell with an edge length of 250 nm and $t_{\mathrm{rel}} = 50\,\%$. The external field $\vec{H}_{\mathrm{ext}}$ is applied along the x-direction. For selected points (a)-(f) magnetization patterns are shown from an on-top perspective: (a) as the external field is reduced a flower state develops. (b) Switch to a C state at very low fields. (c) An asymmetric vortex configuration is formed at remanence. (d) At a low negative field the vortex core moves to the opposite side. (e) Vortex core subsequently moves down the side. (f) After the annihilation of the vortex core a reversed flower state becomes stable.

becomes unstable and switches to the onion-like configuration (see figures 11c and d). This transition leads to a distinctive kink in the hysteresis curve and therefore may well be identifiable in an experiment. For larger structures the reversal along the z-direction happens via the asymmetric vortex configuration. Figure 12 gives a corresponding example for a full pyramid (t_{rel}=100%). The hysteresis curve only contains subtle indications of changes in the micromagnetic configuration. Due to the discrepancy between the structure sizes accessible by experiment ($\sim \mu$m) and simulation ($\sim 100\,$nm), a comparison with the experimentally measured hysteresis curve of figure 1 is currently not feasible [21]. Interestingly the experimental curve exhibits a more square-like shape. This could be due to a pinning of the magnetization, which may arise from the polycrystalline structure of the shell and additional anisotropies (enhanced magnetocrystalline anisotropy of nickel at low temperatures, strain-induced anisotropy) not included in the used model. Another possible explanation is that the reversal involves the nucleation and propagation of domain walls, which may get pinned at imperfections of the sample, such as grain boundaries [21].

Varying the external magnetic field along the x-direction, we again find two reversal mechanisms. For smaller (i.e. $a = 100$ and $150\,$nm) or thin structures (t_{rel}=10 %), we find a direct transition between quasi-homogeneous states (i.e. flower, C and S states). This results in rectangular-shaped hysteresis curves similar to those of Stoner-Wohlfarth particles. Geometries with an edge length of $a = 250\,$nm and thicknesses of $t_{\mathrm{rel}} = 50 \mathrm{and} 100\,\%$ exhibit a reversal mechanism that comprises a transition between two asymmetric vortex states whose cores end on opposing side faces (see figures 13c and d). The switching between the asymmetric vortex states can easily be understood, as both states have a relatively large magnetization component either parallel or anti-parallel to the external field. Generally, the reversal mechanism resembles the one observed for circular nanodots [9]. The main difference, however, is that for the pyramidal shells the hysteresis curve passes through two different remanent states, which correspond to the asymmetric states on opposite side faces. According to figure 13, this transition occurs at relatively low fields, i.e. at fields below our step width of $7958\,\mathrm{Am}^{-1}$. Due to the fourfold symmetry of the pyramidal shell, one cannot only switch between two but four equivalent asymmetric vortex states.

5. Conclusions

We have used micromagnetic simulations to conduct an in-depth analysis on the micromagnetic behaviour of pyramidal core-shell structures in the limit of soft magnetic materials. We have identified and characterized several stable and metastable states in a regime of sizes below $60 \cdot l_{\mathrm{exch}}$. A phase diagram, which presents the energetic ground states at different structure sizes and shell thicknesses, with accurately computed phase boundaries has been created. By carefully examining the results of our micromagnetic simulations we have been able to qualitatively understand the phase transitions between different ground states. Additionally, we have investigated the stability regimes of all

occurring states at different thicknesses. From our findings we conclude that the physics changes crucially in the limit of very thin shells. This implies a higher number of metastable states, generally extended stability regimes of quasi-homogeneous and vortex states (especially towards larger sizes) and differences in the ground state configurations. In particular, the reduction of metastable states with increasing thickness may be technologically relevant as the occurrence of metastable states can lead to problems. Analysing the magnetic reversal with respect to selected directions, we have found a switching mechanism between two equivalent vortex states that can be induced with low magnetic fields.

Acknowledgments

This work has received funding from the Engineering and Physical Sciences Research Council (EPSRC) UK (EP/E040063/1,EP/E039944/1) and from the European Community's Seventh Framework Programme (FP7/2007-2013) under grant agreement no. 233552 (DYNAMAG project). We also thank Richard Boardman and Christoph Hassel for helpful comments.

References

[1] R P Cowburn. Property variation with shape in magnetic nanoelements. *Journal of Physics D: Applied Physics*, 33(1):R1–R16, 2000.

[2] J. I. Martín, J. Nogués, Kai Liu, J. L. Vicent, and Ivan K. Schuller. Ordered magnetic nanostructures: fabrication and properties. *Journal of Magnetism and Magnetic Materials*, 256(1-3):449 – 501, 2003.

[3] Nisha Shukla, Chao Liu, and A.G. Roy. Oriented self-assembly of cubic FePt nanoparticles. *Materials Letters*, 60(8):995 – 998, 2006.

[4] D. Ung, L. D. Tung, G. Caruntu, D. Delaportas, I. Alexandrou, I. A. Prior, and N. T. K. Thanh. Variant shape growth of nanoparticles of metallic fe-pt, fe-pd and fe-pt-pd alloys. *CrystEngComm*, 11:1309–1316, March 2009.

[5] R. P. Cowburn and M. E. Welland. Micromagnetics of the single-domain state of square ferromagnetic nanostructures. *Phys. Rev. B*, 58(14):9217–9226, October 1998.

[6] D. Goll, G. Schütz, and H. Kronmüller. Critical thickness for high-remanent single-domain configurations in square ferromagnetic thin platelets. *Phys. Rev. B*, 67(9):094414, Mar 2003.

[7] H. Kronmüller, D. Goll, R. Hertel, and G. Schütz. Critical thicknesses of domain formations in cubic particles and thin films. *Physica B: Condensed Matter*, 343(1-4):229 – 235, 2004.

[8] Mei-Feng Lai and Chun-Neng Liao. Size dependence of c and s states in circular and square permalloy dots. *Journal of Applied Physics*, 103(7):07E737, 2008.

[9] R. P. Cowburn, D. K. Koltsov, A. O. Adeyeye, M. E. Welland, and D. M. Tricker. Single-domain circular nanomagnets. *Phys. Rev. Lett.*, 83(5):1042–1045, August 1999.

[10] Jonathan Kin Ha, Riccardo Hertel, and J. Kirschner. Micromagnetic study of magnetic configurations in submicron permalloy disks. *Phys. Rev. B*, 67(22):224432, June 2003.

[11] M. E. Schabes and H. N. Bertram. Magnetization processes in ferromagnetic cubes. *Journal of Applied Physics*, 64(3):1347–1357, 1988.

[12] W. Rave, K. Fabian, and A. Hubert. Magnetic states of small cubic particles with uniaxial anisotropy. *Journal of Magnetism and Magnetic Materials*, 190:332 – 348, 1998.

[13] Carlos J. Garca-Cervera, Zydrunas Gimbutas, and Weinan E. Accurate numerical methods

for micromagnetics simulations with general geometries. *Journal of Computational Physics*, 184(1):37 – 52, 2003.

[14] C. A. Ross, M. Farhoud, M. Hwang, Henry I. Smith, M. Redjdal, and F. B. Humphrey. Micromagnetic behavior of conical ferromagnetic particles. *Journal of Applied Physics*, 89(2):1310–1319, 2001.

[15] R. P. Boardman, H. Fangohr, M. J. Fairman, J. Zimmermann, S. J. Cox, A. A. Zhukov, and P. A.J. de Groot. Micromagnetic modelling of ferromagnetic cones. *Journal of Magnetism and Magnetic Materials*, 312(1):234 – 238, 2007.

[16] Richard P. Boardman, Hans Fangohr, Simon J. Cox, Alexander V. Goncharov, Alexander A. Zhukov, and Peter A. J. de Groot. Micromagnetic simulation of ferromagnetic part-spherical particles. *Journal of Applied Physics*, 95(11):7037–7039, 2004.

[17] Richard P. Boardman, Jürgen Zimmermann, Hans Fangohr, Alexander A. Zhukov, and Peter A. J. de Groot. Micromagnetic simulation studies of ferromagnetic part spheres. *Journal of Applied Physics*, 97(10):10E305, 2005.

[18] W. Williams, A. R. Muxworthy, and G. A. Paterson. Configurational anisotropy in single-domain and pseudosingle-domain grains of magnetite. *J. Geophys. Res.*, 111(B12S13), 2006.

[19] R. Hertel, O. Fruchart, S. Cherifi, P.-O. Jubert, S. Heun, A. Locatelli, and J. Kirschner. Three-dimensional magnetic-flux-closure patterns in mesoscopic fe islands. *Phys. Rev. B*, 72(21):214409, December 2005.

[20] D. Goll, A. E. Berkowitz, and H. N. Bertram. Critical sizes for ferromagnetic spherical hollow nanoparticles. *Phys. Rev. B*, 70(18):184432, November 2004.

[21] F. Nasirpouri, M. Engbarth, S. J. Bending, L. M. Peter, A. Knittel, and H. Fangohr. Growth and magnetisation of highly-faceted three-dimensional ferromagnetic/non-ferromagnetic core/shell structures. submitted.

[22] H. Kronmüller and Manfred Fähnle. *Micromagnetism and the Microstructure of Ferromagnetic Solids*. Cambridge University Press, 2003.

[23] T. Fischbacher, M. Franchin, G. Bordignon, and H. Fangohr. A systematic approach to multiphysics extensions of finite-element-based micromagnetic simulations: Nmag. *Magnetics, IEEE Transactions on*, 43(6):2896–2898, June 2007.

[24] D.R. Fredkin and T.R. Koehler. Hybrid method for computing demagnetizing fields. *Magnetics, IEEE Transactions on*, 26(2):415–417, Mar 1990.

[25] W. Hackbusch. A sparse matrix arithmetic based on $\mathcal{H}$-matrices. part i: Introduction to $\mathcal{H}$-matrices. *Computing*, 62:89–108, 1999.

[26] S. Börm and L. Grasedyck. Hybrid cross approximation of integral operators. *Numerische Mathematik*, 101:221 – 249, 2005.

[27] A. Knittel, M. Franchin, G. Bordignon, T. Fischbacher, S. Bending, and H. Fangohr. Compression of boundary element matrix in micromagnetic simulations. *Journal of Applied Physics*, 105(7):07D542, 2009.

[28] W. Rave, K. Ramstöck, and A. Hubert. Corners and nucleation in micromagnetics. *Journal of Magnetism and Magnetic Materials*, 183(3):329 – 333, 1998.

[29] A. Raizer, S. R. H. Hoole, G. Meunier, and J.-L. Coulomb. p- and h-type adaptive mesh generation. *Journal of Applied Physics*, 67(9):5803–5805, 1990.

[30] M. J. Donahue. A variational approach to exchange calculations in micromagnetics. *Journal of Applied Physics*, 83(11):6491–6493, 1998.

[31] H.H. Long, E.T. Ong, Z.J. Liu, and E.P. Li. Fast fourier transform on multipoles for rapid calculation of magnetostatic fields. *Magnetics, IEEE Transactions on*, 42(2):295 – 300, feb. 2006.

[32] D. Suess, V. Tsiantos, T. Schrefl, J. Fidler, W. Scholz, H. Forster, R. Dittrich, and J. J. Miles. Time resolved micromagnetics using a preconditioned time integration method. *Journal of Magnetism and Magnetic Materials*, 248(2):298 – 311, 2002.

[33] A. C. Hindmarsh, P. N. Brown, K. E. Grant, S. L. Lee, R. Serban, D. E. Shumaker, and C. S.

Woodward. Sundials: Suite of nonlinear and differential/algebraic equation solvers. *ACM Transactions on Mathematical Software*, 31(3):363, 2005.

[34] A. R. Muxworthy and W. Williams. Critical single-domain/multidomain grain sizes in noninteracting and interacting elongated magnetite particles: Implications for magnetosomes. *J. Geophys. Res.*, 111(B12S12), 2006.

[35] J. Miltat and A. Thiaville. FERROMAGNETISM: Vortex Cores-Smaller Than Small. *Science*, 298(5593):555–, 2002.

[36] R. P. Cowburn and M. E. Welland. Phase transitions in planar magnetic nanostructures. *Applied Physics Letters*, 72(16):2041–2043, 1998.

[37] A. Wachowiak, J. Wiebe, M. Bode, O. Pietzsch, M. Morgenstern, and R. Wiesendanger. Direct Observation of Internal Spin Structure of Magnetic Vortex Cores. *Science*, 298(5593):577–580, 2002.